Elucidating the Oxygen Storage-Release Dynamics in Ceria Nanorods by Combined Multi-Wavelength Raman Spectroscopy and DFT

Marc Ziemba[1], M. Verónica Ganduglia-Pirovano[2], Christian Hess[1*]

[1]Eduard-Zintl-Institute of Inorganic and Physical Chemistry, Technical University of Darmstadt, Alarich-Weiss-Str. 8, 64287 Darmstadt, Germany

*email: christian.hess@tu-darmstadt.de

[2]Instituto de Catálisis y Petroleoquímica - Consejo Superior de Investigaciones Científicas, Marie Curie 2, 28049 Madrid, Spain

Abstract

The oxygen storage-release dynamics in ceria nanorods is elucidated by using a combination of *in situ* multi-wavelength Raman spectroscopy and DFT calculations. Ceria nanorods exposing CeO_2(100) and CeO_2(110) facets are shown to be characterized by highly facet-dependent properties regarding molecular oxygen activation and decomposition as well as lattice oxygen dynamics. Temperature-dependent Raman results show that oxygen is stored in the form of peroxide species on the (100) facets which are then released as gaseous oxygen, whereas lattice oxygen is involved with the (110) facets. On the latter, peroxide species first decompose into oxygen atoms that heal vacant lattice oxygen sites before being released as gaseous oxygen. The exposure of different facets makes ceria nanorods an interesting material for catalytic applications, because they allow the use of a mixture of oxygen storage-release functions, as well as their synergistic interactions, in a single system.

Table of Contents Graphic

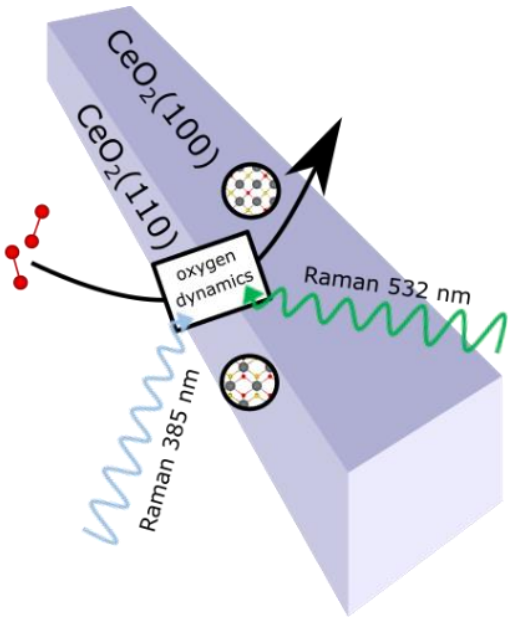

Keywords

Ceria nanorods, surface termination, *in situ* Raman spectroscopy, DFT, oxygen activation, oxygen storage

Ceria is an important support material for precious metals in oxidation reactions such as the CO oxidation or the water-gas shift reaction.[1–4] It is therefore of great interest to understand the reduction and re-oxidation of the support during reaction. In addition, ceria is used as an oxygen storage component in the formulation of automotive catalysts. Whereas the choice of the surface facet has been shown to have a strong effect on the oxygen storage capacity,[5,6] a detailed understanding of the oxygen storage properties of nanostructured ceria is still missing. In the context of ceria materials, Raman spectroscopy has proved to be a powerful method to detect adsorbed oxygen species or oxygen defects.[7–12] In previous studies, the dependence of oxygen activation on the exposed ceria facet has been investigated employing single crystal surfaces,[13] while we have addressed catalytically interesting ceria powder samples with either CeO_2(111) or CeO_2(100) surface termination.[8] Our previous study has revealed a facet-dependent behavior regarding oxygen adsorption and activation, resulting in the formation of peroxide (O_2^{2-}), superoxides (O_2^-), and weakly bound oxygen ($O_2^{\delta-}$) species.[8] The relevance of investigating the adsorption of O_2 species on ceria surfaces lies in the fact that O_2 species not only serve as probe a molecule, as e.g. CO,[14] but may also be involved in the dynamic exchange of lattice oxygen and the catalytic activity of ceria-based systems.[1,4,15–18]

In this work, we study the facet-dependent oxygen adsorption, activation and dynamics at ceria rods, exposing (110) and (100) facets, employing a combined multi-wavelength Raman / DFT approach, where our previous study on ceria nanocubes serves as a reference for the (100) facet.[8] We show that the oxygen storage-release mechanism depends largely on the exposed facet and is related to differences in the molecular oxygen activation and decomposition properties as well as in the ease of formation of lattice oxygen vacancies.

Based on the growth mechanism of ceria rods and findings from the literature, we know that the proportion of both (110) and (100) facets is significant, whereby that of the former is slightly higher.[19] The (110) facet has been shown to be the facet with the lowest surface oxygen defect formation energy.[13,20–22] Thus, this facet is particularly interesting for reactions in which lattice oxygen is involved. After the hydro-thermal synthesis of the ceria rods (for details see SI), they were characterized using TEM, XRD and N_2 adsorption at 77 K. The TEM images in Figure 1A and Figure S2 demonstrate the successful synthesis of ceria rods containing (100) and (110) surface terminations, based on the observed distances between lattice planes of 0.27 nm and 0.19 nm, respectively.[23,24] Using FFT of the individual domains and masking the diffraction patterns with subsequent inverse FFT, the surface terminations were analyzed in more detail (see Figures S3 and S4). To exclude the presence of the (111) surface termination,

Raman spectroscopy with an excitation wavelength of 385 nm was used as a more integral method than TEM. Comparing the spectra of the rods with those of particles exhibiting a (111) termination reveals, that the rods do not show the characteristic transversal surface mode of the (111) surface at around 402 cm^{-1}, in contrast to the sheets and polyhedra (see Figure S5).[7] The XRD results show that only cubic CeO_2 is present (see Figure S6). Using N_2 adsorption and the BET model, a specific surface area of 88 m^2/g and a pore volume of 0.22 cm^3/g were determined (for isotherms see Figure S7) and by means of the BJH model an average pore diameter of 28 nm could be determined (see Figure S8). Our previous detailed TEM analysis has confirmed that the morphology and size of the particles does not change during exposure to water-gas shift conditions, which are much harsher than the conditions applied in this study.[17] Thus, we can safely assume that the surface termination and the shape of the particles are preserved during the here performed experiments.

Multi-wavelength Raman spectroscopy with excitation wavelengths of 385 and 532 nm was employed to monitor the oxygen dynamics of the ceria rods, where the penetration depth at 385 nm is less than that at 532 nm, and since ceria shows absorption at 385 nm, a selective (resonance) enhancement of the ceria-related vibrational modes is possible. The use of an additional visible excitation wavelength (633 nm; see Figure S9) does not provide any fundamentally new insight compared to 532 nm excitation, in contrast to the 385 nm spectrum, as described in the following. The *in situ* Raman spectra of ceria nanorods in 25 % O_2 at room temperature are shown in Figures 1B and 1C. In the 385 nm Raman spectrum (see Figure 1B), due to the resonance enhancement, the defect band at 600 cm^{-1} is more intense than the F_{2g} band at 459 cm^{-1}, indicating the presence of near-surface oxygen defects.[7] The bands at 263 cm^{-1} and 1187 cm^{-1} are assigned to the 2TA and the 2LO overtones, respectively.[7] Furthermore, a peroxide-related band at 835 cm^{-1} appears, which originates from the adsorption of molecular oxygen at surface oxygen vacant sites with the excess electrons located at nearby cerium atoms.[8,13,25] The asymmetry of the 835 cm^{-1} band can be explained by the occurrence of agglomerated peroxides, which are characterized by a blue-shift, as shown previously for the (100) surface, and will be here discussed in more detail for the (110) surface in the context of Figure 2A.[8] In the 385 nm spectrum, a small band at 336 cm^{-1} is observed, which is assigned to the deformation vibration of peroxides on the surface of the ceria rods based on the results of the DFT calculations (see below, Figure 2B). Note that typically this band cannot be observed by visible Raman spectroscopy (532 nm) due to overlays in this region (see Figure 1C), thus making the use of different excitation wavelengths essential.[4] Moreover, it is also noticeable that despite the presence of the CeO_2(100) facet, no or only very weak superoxide bands

(1103 cm^{-1} and/or 1137 cm^{-1})[8] are observed, in contrast to our previous studies on ceria cubes exposing (100) facets only. The absence of superoxide bands strongly suggests that the presence of the (110) facet next to the CeO_2(100) facet modifies the latter, resulting in different properties as compared to those of ceria cubes.

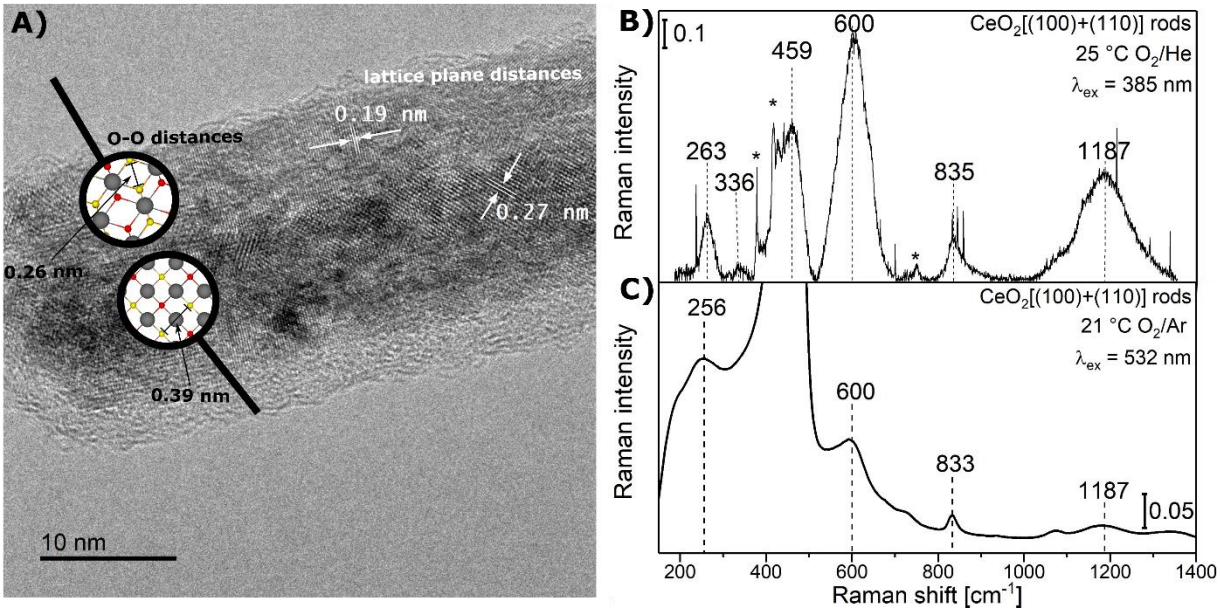

Figure 1: A) TEM image of ceria nanorods. White arrows on the right side indicate the distance of the lattice planes in the direction of the particle surface. The two magnifying glasses on the left side show theoretical top view images of the CeO_2(110) (at the top) and CeO_2(100) (at the bottom) surfaces together with the calculated smallest distance between two surface oxygen atoms (PBE+U/4.5 eV). **B)** *In situ* 385 nm Raman spectrum of ceria nanorods recorded at 25 °C in 25 % O_2/He (pretreatment: 2 h, 120 °C, 25 % O_2/He, 50 mL/min), at a total flow rate of 50 mL/min. The asterisk (*) marks bands originating from the sapphire window, while other sharp features result from cosmic rays. **C)** *In situ* 532 nm Raman spectrum of ceria nanorods recorded at 21 °C in 25 % O_2/Ar, at a total flow rate of 100 mL/min. The high intensity F_{2g} peak at 455.1 cm^{-1} was cut off to allow an enlarged view of the other features.

The adsorption energy of peroxide species, O_2^{2-}, on ceria surfaces is the result of two energy contributions with opposite effects, $E_{ads,O_2^{2-}} = -E_{vac,O} + E_{ads,O}$, namely, the energy gain upon healing the surface vacancies on the reduced facet, $-E_{vac,O} = -[E_{CeO_{2-x}} + \frac{1}{2} E_{O_2} - E_{CeO_2}]$, and the repulsive interactions between the charged chemisorbed species, $E_{ads,O} = E_{O_2^{2-}/CeO_{2-x}} - \frac{1}{2}E_{O_2} - E_{CeO_2}$. $E_{ads,O}$ is the adsorption energy of the resulting O atom on the

corresponding clean facet resulting from the vacancy healing by the peroxide species. In the following, we consider the process of oxygen vacancy formation and healing using the examples of the (100) and (110) surfaces with *c*(2×2) (see Figure S11) and (2×2) periodicity, respectively ($\Theta_{O_{vac}} = \Theta_{O_2^{2-}} = 0.125$). The healing of a surface oxygen vacancy ($-E_{vac,O}$) is an exothermic process on both surfaces, but on the (100) facet the energy released is by about 0.07 eV higher than on the (110) facet (cf. −1.39 eV, Figure S7A and Table S4 in ref 8, and −1.32 eV, Figure S10F and Table S1, respectively), which is in line with corresponding values for the surface oxygen defect formation energy ($+E_{vac,O}$) in the literature.[13] However, the oxygen adsorption energy after the vacancy has been healed by the adsorption of peroxide species, $E_{ads,O}$, is exothermic on the (100) facet (–0.34 eV, see Figure S8A and Table S4 in ref 8) and endothermic on the (110) (+0.15 eV, see Figure S11G and Table S2). As a consequence of the facet-dependent $E_{vac,O}$ and $E_{ads,O}$ energy values, the calculated peroxide adsorption energy on the (100) facet is by 0.56 eV higher than on the (110) one (cf. –1.73 eV, Table S4 in ref 8, and –1.17 eV, Table S2, respectively). Summarizing, on ceria rods, O_2^{2-} species are strongly bound on the (100) facets, and the removal of lattice oxygen is more facile at the (110) facets.

Comparing the O_2^{2-}/CeO_{2-x}(100) and O_2^{2-}/CeO_{2-x}(110) structures at a peroxide coverage of 0.125 ML, we found that the O–O bond length of the chemisorbed O_2^{2-} species on the (110) facet is smaller by 2.3 pm than on the (100) facet (cf. 1.445 Å, (2×2)-(110), Table S2, and 1.468 Å, *c*(2×2)-(100), Table S4 in ref 8), which is in line with previous studies.[13] This difference in bond length, results in a higher stretching vibrational frequency by 30 cm^{-1} for the O_2^{2-} species on the (110) facet compared to those on the (100) one. Thus, the presence of peroxides on the surface of CeO_2 rods exposing both facets, may lead to band broadening due to the facet-dependent O–O bond lengths of the chemisorbed O_2^{2-} species. Moreover, as previously discussed for the (111) and (100) facets,[8] on the (110) one, the O–O bond length also decreases with increasing O_2^{2-} coverage from 0.125 to 1 ML (see Table S2), which is reflected in an increase of the stretching vibrational frequency (see Figure 2A), with the consequent broadening of the peroxide band due to the simultaneous presence of different local coverages. As a special feature of the (110) facet, we found that in the complete peroxide monolayer ($\Theta_{O_2^{2-}} = 1$ ML), two peroxide configurations with different O–O bond lengths exist (see Figure S11E and Table S2), which is reflected in two different vibrational frequencies (indicated as green and blue dots in Figure 2A), that may also contribute to the broadening of

the peroxide band in the experimental spectra. Summarizing these results, the observed band broadening in the experimental spectra for the rods is due to both the presence of different local coverages and the existence of two facets. It should be noted that on the CeO_2(110) surface, the creation of a surface oxygen defect next to an existing peroxide is energetically favorable. For example, a surface oxygen atom from the O_2^{2-}/CeO_{2-x}(110)-(1×1) structure with $\Theta_{O_{vac}} = \Theta_{O_2^{2-}} = 0.5$ (see Figure S11D) is removed for a cost of 1.63 eV, i.e., 0.48 eV less compared to the case without a nearby peroxide (2.11 eV, see Figure S10A and Table S1). For a comparison of our results with previous theoretical studies,[26,27] see the Supporting Information.

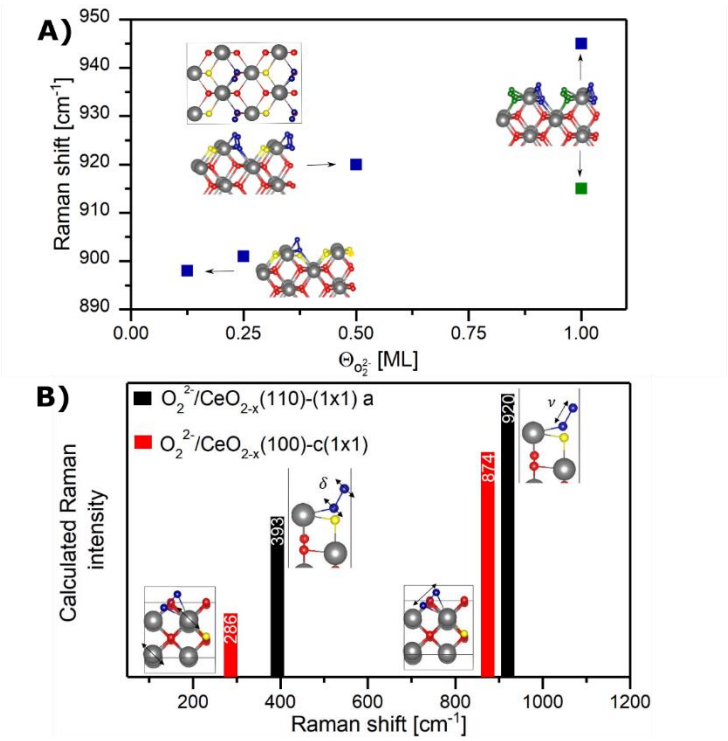

Figure 2: A) Relationship between the coverage and the Raman shift of peroxides species on the CeO_2(110) facet, based on the most stable structures for coverages of $\Theta_{O_2^{2-}} = 0.125$, 0.25, 0.5, and 1 ML (see Figures S11G, F, A, and E, respectively). Surface oxygen is shown in yellow, cerium atoms in gray, and lattice oxygen in red. For the 1 ML structure, the two different peroxide species are shown in green and blue. **B)** Calculated Raman intensities for the most stable peroxide structure at 0.5 ML coverage on CeO_2(110) with (1×1) periodicity (black) (see Figure S11A) and on CeO_2(100) with *c*(1×1) periodicity (red), according to our previous study.[8] The symmetry (δ, υ) of the vibrations is indicated.

Moreover, Figure 2B shows that for peroxides on ceria surfaces, besides the O–O stretching vibration, another vibration occurs at lower wavenumbers, which is also Raman-active but less intense than the stretching vibration. Note that this vibration is observed for all peroxide coverages (not shown). The symmetry of this vibration can be best described as a deformation vibration (δ). Both the stretching and deformation vibrations of O_2^{2-} species on the (100) facet are at significantly lower wavenumbers compared to those on the (110). Based on the above-mentioned higher stability of the O_2^{2-} species on the CeO_2(100) facet, we assigned the experimentally observed band at 336 cm^{-1} on CeO_2 rods (see Figure 1B) to peroxide deformation vibrations of species predominantly adsorbed on the (100) facets. While a band and a shoulder have previously been reported for CeO_2(111), at 357 and 340 cm^{-1}, respectively, no clear assignment was provided.[11]

On the CeO_2(110) facets, for which peroxide species are weaker bound as compared to the (100) facets, a more facile dissociation of the peroxide species after O_2 adsorption at an oxygen vacant site is expected, where the resulting oxygen atoms heal adjacent oxygen vacancies, consistent with the behavior observed previously for single crystals.[13] As discussed above, it is likely that surface oxygen vacancies would form in the immediate neighborhood of adsorbed peroxide species on the (110) facets. This would also occur on the (100) facets.[8] For instance, the removal of a surface oxygen atom from the O_2^{2-}/CeO_{2-x}(100)-c(1×1) structure with $\Theta_{O_{vac}} = \Theta_{O_2^{2-}} = 0.5$ is by 0.45 eV energetically less costly compared to the case without a nearby peroxide (cf. 2.13 and 1.68 eV, respectively[8]). However, two factors would favor the breakage of the O_2^{2-} species into two O atoms on the (110) facets compared to the (100) ones, namely, the closer distance by 1.3 Å between anionic surface sites on the former (see Figure 1A), as well as the higher exothermicity of the reaction leading to the re-oxidation of the surface (e.g., the reaction energy of O_2^{2-}/CeO_{2-x} ($\Theta_{O_{vac}} = 1, \Theta_{O_2^{2-}} = 0.5$) → CeO_2 equals to −1.895 and −1.360 eV for the (110) and (100) facets, respectively). Consequently, we conclude that the observed peroxides on the rods mostly originate from peroxides adsorbed on the (100) facets. In this context, it is worth mentioning that previous theoretical studies have shown that oxygen vacancy migration in bulk ceria[28–30] and at the (111) surface[31] can occur with barriers below 0.5 eV. Oxygen vacancy migration is not just conceivable on the (110) and (100) facets, but is likely to play an important role after peroxide dissociation occurs.

Figure 3 shows the temperature-dependent oxygen activation and dynamics for rods (A) and cubes (B), as probed by the formation of peroxides/superoxides species and the F_{2g} shift, as a measure of near-surface oxygen defects. For the *ex situ* measurement at 21 °C, the F_{2g} band position for the ceria rods is at 454.3 cm^{-1} (see Figure 3A) corresponding to a red-shift of ~10 cm^{-1} as compared to ceria cubes exposing (100) facets (464.0 cm^{-1}, see Figure 3B). This red-shift is indicative of a high defect concentration in the rods,[32] in line with the observed small intensity of the F_{2g} band (451.1 cm^{-1}) and the strong defect band at 600 cm^{-1} when using a 385 nm excitation (see Figure 1B), as well as with the greatest ease with which oxygen defects can be created on the (110) facet. It should be noted that the position of the F_{2g} band varies if different excitation wavelengths are used, which can be related to the associated different penetration depths. In fact, if 532 nm excitation is employed for *in situ* Raman measurements on rods, the F_{2g} band is red-shifted by 3.9 cm^{-1} (455.1 cm^{-1}, see Figures 1C and 3A) compared to the position observed at 385 nm excitation (459 cm^{-1}, see Figure 1B). For an excitation wavelength of 532 nm, due to weaker absorption,[4] the laser penetrates deeper into the sample increasing the contribution of subsurface layers.[33] Thus, the observed red-shift of the F_{2g} band at 532 nm excitation indicates that the subsurface of the rods is also defect-rich.

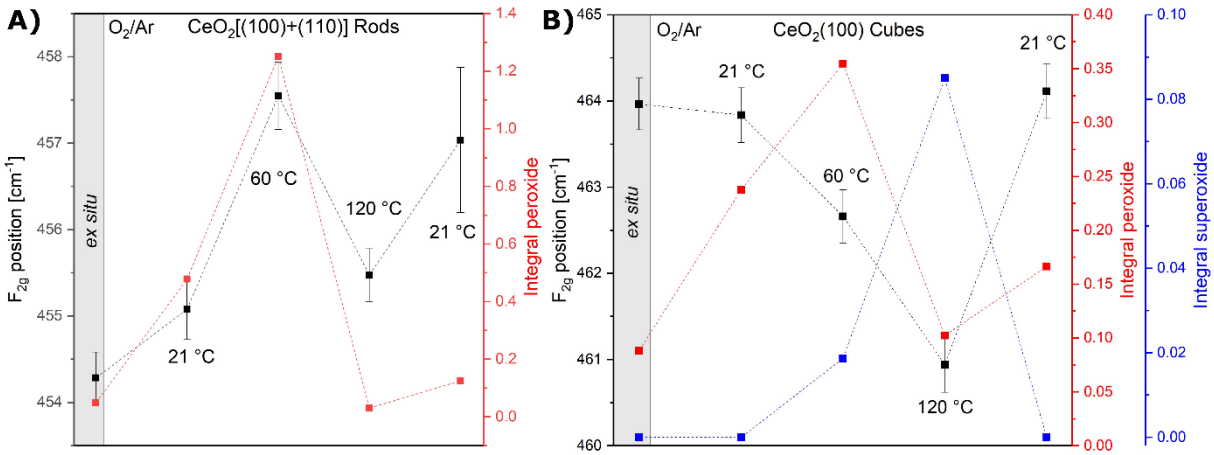

Figure 3: A) Temperature-dependent Raman F_{2g} position and peroxide integral for ceria rods at 532 nm excitation. **B)** Raman F_{2g} position, peroxide, and superoxide integrals for ceria cubes at 532 nm excitation based on previous data.[8] The data points for *in situ* conditions correspond to the mean value of three measurements. Inaccuracies of the F_{2g} position are given as standard deviations. The scaling range for the F_{2g} positions is the same for rods and cubes.

Furthermore, Figure 3 shows that the F_{2g} position varies with temperature. According to previous studies,[34] an increase in temperature leads to a red-shift of the F_{2g} band. However,

within the temperature range considered here, those changes are small (<1 cm^{-1}) and thus within the experimental error. Hence, a temperature effect alone cannot explain the observed changes of the F_{2g} band position (see Figure 3). When switching the temperature from 21 °C to 60 °C, a blue-shift of 2.3 cm^{-1} is observed for the rods and a red-shift of 1.2 cm^{-1} for the cubes, indicating ceria oxidation and reduction, respectively.[7] At the same time, for both rods and cubes, the peroxide band shows its maximum intensity. The increase in the amount of adsorbed peroxide species as the temperature increases from 21 ºC to 60 ºC, is related to the above-discussed ease with which oxygen vacancies can be created close to an existing peroxide on both surfaces. Peroxide species bind at those vacant sites on both surfaces, which is consistent with the observed maximum intensity of the peroxide bands (see Figure 3). However, as stated above, the stability of peroxide species on the different facets is *not* the same.

Referring back to the DFT data and our previous argument, peroxides on (100) facets are stronger bound than on (110) ones, and peroxide dissociation – followed by healing of lattice oxygen vacancies– is more exothermic on the (110) facets. Thus, we here propose that on ceria rods exposing (110) and (100) facets, two different oxygen storage mechanisms operate simultaneously as follows. The weaker bound peroxide species on the (110) facets decompose and oxygen atoms are stored in the lattice, which is in line with the observed blue-shift of the F_{2g} band (see Figure 3A). At the same time, oxygen is also stored in the form of chemisorbed O_2^{2-} species on the (100) facets of the rods. Conversely, for the cubes, exposing solely (100) facets, as the temperature increases from 21 ºC to 60 ºC, oxygen vacancies are created near the surface and O_2^{2-} species strongly adsorb (i.e., are stored) on those vacant sites on the surface, but the deeper layers remain reduced because the O_2^{2-} species do not decompose, which is consistent with the observed red-shift of the F_{2g} band (see Figure 3B). We turn now to the question of oxygen release from rods and cubes.

When the temperature of the rods is further increased up to 120 °C, a red-shift of 2.0 cm^{-1} is observed (see Figure 3A), indicating the onset of ceria reduction, and simultaneously, the peroxide band fully loses intensity. Moreover, the F_{2g} position is slightly blue-shifted by 0.3 cm^{-1} as compared to the initial position at 21 ºC, indicating that comparatively, the system is oxidized. What is happening is that all of the stored oxygen in the form of O_2^{2-} on the (100) facets is released as gaseous oxygen, consistent with the loss in intensity of the peroxide band, although part of the oxygen stored in the lattice is also released. Such operating release mechanisms leave near-surface oxygen vacant sites and that is why a red-shift of the F_{2g} band is observed as the temperature increases from 60 ºC to 120 ºC. The fact that the F_{2g} position at 120 ºC is slightly blue-shifted compared to that at 21 ºC indicates that some of the stored oxygen

in the lattice at 60º C, for which the existence of the (110) facets is essential, has not been removed at 120 ºC. We note that as a result of the oxidative treatment, the initial reduced state is not recovered after cooling the sample down to 21 °C.

As the temperature is raised from 60 ºC to 120 ºC, the cubes, exposing exclusively (100) facets, behave once more differently than the rods (cf. Figure 3A and 3B). The peroxide band loses intensity and a red-shift of the F_{2g} band is observed (1.7 cm^{-1}), but differently from the rods, superoxides, O_2^-, are formed on the cubes. Hence, the stored oxygen in the form of O_2^{2-} on the (100) surfaces of the cubes is converted into O_2^- species, and it is the release of lattice oxygen what is consistent with the red-shift of the F_{2g} band. Based on this observation, we propose that at higher temperatures on the cubes a thermal equilibrium between O_2^{2-} and O_2^- species exists and that these species do not decompose, which is related to the high stability of peroxides/superoxides on the (100) surface. However, if we now compare the stability of the O_2^{2-} species on the (100) surfaces of the cubes with that of the O_2^{2-} species on the (100) facets of the rods (cf. Figure 3A and 3B), we realize that on the cubes there is a $O_2^{2-} \leftrightarrow O_2^-$ conversion, whereas on the rods, O_2^{2-} species are released as gaseous oxygen. This reveals that there are synergistic interactions between the existing (100) and (110) facets in the rods, which make the former behave differently than in the absence of (110) facets, as in case of the cubes.

Summarizing, a combined *in situ* multi-wavelength Raman and DFT approach has been employed to elucidate the oxygen storage-release mechanism on ceria nanorods. It is shown that the molecular oxygen activation, decomposition and oxygen dynamics in ceria nanorods is quite complex due to the presence of two ceria facets. Peroxide formation on the (100) facets is energetically favored over the (110) facets, whereas the opposite behavior is observed for defect formation. Both facets are proposed to contribute to oxygen storage either by formation of active oxygen species, such as peroxides, or by incorporation of lattice oxygen. Moreover, using a combination of DFT calculations and Raman spectroscopy, the band at 336 cm^{-1} (see Figures 1 and 2) could be univocally assigned to the deformation vibration of peroxides on (100).

Generally speaking, the understanding of the oxygen-release storage mechanisms in ceria-based systems is of great importance for catalytic applications. Moreover, it is known that the ceria surface structure may alter the catalytic activity of ceria-based catalysts, and thus, ceria nanocrystals with controlled morphologies, such as nanocubes and nanorods are fabricated. The coexistence of the (100) and (110) facets is assumed to be responsible for the excellent oxygen

storage capacity of ceria rods, as demonstrated previously by experiment,[5,6,23] but not understood in detail. The microscopic understanding gained in this study reveals that in ceria rods, two different oxygen-release storage mechanisms operate simultaneously. Oxygen can be stored in the form of activated oxygen or as lattice oxygen at low temperatures (<100 °C), which will be released at higher temperatures (>100ºC). Activated peroxide species adsorb on both facets but the dynamics of such species with varying temperature depend on the facet. Whereas on the (100) facets the strongest bound peroxide species are initially stored and leave the surface as gaseous oxygen, on the (110), the creation of near-surface vacancies is easier and the weakest bound peroxide species decompose into oxygen atoms that fill the vacancies, which then are also released as gaseous oxygen. Thus, ceria rods enable a combination of different oxygen storage and activation functions. Our results should be useful in the design of systems with improved storage capacity.

Acknowledgements

The DFT calculations were conducted using the Lichtenberg high performance computer of the TU Darmstadt. Jochen Rohrer and Karsten Albe are acknowledged for support with the VASP code. We thank Stefan Lauterbach and Hans-Joachim Kleebe for TEM measurements, Martin Brodrecht for BET measurements, Kathrin Hofmann for XRD measurements, Simone Rogg for *in situ* Raman measurements at 385 nm excitation, and Patricia Pérez-Bailac and Pablo G. Lustemberg for helpful discussions on the CeO_2(110) vacancy structure. M.V.G.P. acknowledges support by the MICINN-Spain (project no. RTI2018-101604-B-I00).

Supporting Information

Detailed information on experimental and theoretical methods as well as additional theoretical data for peroxide species on the reduced CeO_2(110) surface and a comparison of the O_2^{2-}/CeO_{2-x}(110) and O_2^{2-}/CeO_{2-x}(100) structures with work in the literature.

References

(1) Trovarelli, A.; Llorca, J. Ceria Catalysts at Nanoscale: How Do Crystal Shapes Shape Catalysis? *ACS Catal.* **2017**, *7* (7), 4716–4735.

(2) Fu, Q.; Saltsburg, H.; Flytzani-Stephanopoulos, M. Active Nonmetallic Au and Pt Species on Ceria-Based Water-Gas Shift Catalysts. *Science* **2003**, *301* (5635), 935–938.

(3) Schilling, C.; Ziemba, M.; Hess, C.; Ganduglia-Pirovano, M. V. Identification of Single-Atom Active Sites in CO Oxidation over Oxide-Supported Au Catalysts. *J. Catal.* **2020**, *383*, 264–272.

(4) Ziemba, M.; Hess, C. Influence of Gold on the Reactivity Behaviour of Ceria Nanorods in CO Oxidation: Combining Operando Spectroscopies and DFT Calculations. *Catal. Sci. Technol.* **2020**, *10* (11), 3720–3730.

(5) Li, J.; Zhang, Z.; Tian, Z.; Zhou, X.; Zheng, Z.; Ma, Y.; Qu, Y. Low Pressure Induced Porous Nanorods of Ceria with High Reducibility and Large Oxygen Storage Capacity: Synthesis and Catalytic Applications. *J. Mater. Chem. A* **2014**, *2* (39), 16459–16466.

(6) Ishikawa, Y.; Takeda, M.; Tsukimoto, S.; Nakayama, K. S.; Asao, N. Cerium Oxide Nanorods with Unprecedented Low-Temperature Oxygen Storage Capacity. *Adv. Mater.* **2016**, *28* (7), 1467–1471.

(7) Schilling, C.; Hofmann, A.; Hess, C.; Ganduglia-Pirovano, M. V. Raman Spectra of Polycrystalline CeO_2: A Density Functional Theory Study. *J. Phys. Chem. C* **2017**, *121* (38), 20834–20849.

(8) Schilling, C.; Ganduglia-Pirovano, M. V.; Hess, C. Experimental and Theoretical Study on the Nature of Adsorbed Oxygen Species on Shaped Ceria Nanoparticles. *J. Phys. Chem. Lett.* **2018**, *9* (22), 6593–6598.

(9) Taniguchi, T.; Watanabe, T.; Sugiyama, N.; Subramani, A. K.; Wagata, H.; Matsushita, N.; Yoshimura, M. Identifying Defects in Ceria-Based Nanocrystals by UV Resonance Raman Spectroscopy. *J. Phys. Chem. C* **2009**, *113* (46), 19789–19793.

(10) Agarwal, S.; Zhu, X.; Hensen, E. J. M.; Mojet, B. L.; Lefferts, L. Surface-Dependence of Defect Chemistry of Nanostructured Ceria. *J. Phys. Chem. C* **2015**, *119* (22), 12423–12433.

(11) Pushkarev, V. V.; Kovalchuk, V. I.; D'Itri, J. L. Probing Defect Sites on the CeO_2 Surface with Dioxygen. *J. Phys. Chem. B* **2004**, *108* (17), 5341–5348.

(12) Choi, Y. M.; Abernathy, H.; Chen, H.-T.; Lin, M. C.; Liu, M. Characterization of O_2–

CeO_2 Interactions Using In Situ Raman Spectroscopy and First-Principle Calculations. *ChemPhysChem* **2006**, *7* (9), 1957–1963.

(13) Yang, C.; Yu, X.; Heißler, S.; Weidler, P. G.; Nefedov, A.; Wang, Y.; Wöll, C.; Kropp, T.; Paier, J.; Sauer, J. O_2 Activation on Ceria Catalysts-The Importance of Substrate Crystallographic Orientation. *Angew. Chem. Int. Ed.* **2017**, *56* (51), 16399–16404.

(14) Yang, C.; Yu, X.; Heißler, S.; Nefedov, A.; Colussi, S.; Llorca, J.; Trovarelli, A.; Wang, Y.; Wöll, C. Surface Faceting and Reconstruction of Ceria Nanoparticles. *Angew. Chem. Int. Ed.* **2017**, *56* (1), 375–379.

(15) Lohrenscheit, M.; Hess, C. Direct Evidence for the Participation of Oxygen Vacancies in the Oxidation of Carbon Monoxide over Ceria-Supported Gold Catalysts by Using Operando Raman Spectroscopy. *ChemCatChem* **2016**, *8* (3), 523–526.

(16) Guzman, J.; Carrettin, S.; Corma, A. Spectroscopic Evidence for the Supply of Reactive Oxygen during CO Oxidation Catalyzed by Gold Supported on Nanocrystalline CeO_2. *J. Am. Chem. Soc.* **2005**, *127* (10), 3286–3287.

(17) Ziemba, M.; Ganduglia-Pirovano, V.; Hess, C. Insight into the Mechanism of the Water-Gas Shift Reaction over Au/CeO_2 Catalysts Using Combined Operando Spectroscopies. *Faraday Discuss.* **2020**. https://doi.org/10.1039/C9FD00133F.

(18) Kim, H. Y.; Henkelman, G. CO Oxidation at the Interface between Doped CeO_2 and Supported Au Nanoclusters. *J. Phys. Chem. Lett.* **2012**, *3* (16), 2194–2199.

(19) Liu, Z.; Li, X.; Mayyas, M.; Koshy, P.; Hart, J. N.; Sorrell, C. C. Growth Mechanism of Ceria Nanorods by Precipitation at Room Temperature and Morphology-Dependent Photocatalytic Performance. *CrystEngComm* **2017**, *19* (32), 4766–4776.

(20) Kullgren, J.; Hermansson, K.; Castleton, C. Many Competing Ceria (110) Oxygen Vacancy Structures: From Small to Large Supercells. *J. Chem. Phys.* **2012**, *137* (4), 044705.

(21) Wu, Z.; Overbury, S. H. *Catalysis by Materials with Well-Defined Structures*; Elsevier, 2015.

(22) Nolan, M.; Parker, S. C.; Watson, G. W. The Electronic Structure of Oxygen Vacancy Defects at the Low Index Surfaces of Ceria. *Surf. Sci.* **2005**, *595* (1–3), 223–232.

(23) Mai, H.-X.; Sun, L.-D.; Zhang, Y.-W.; Si, R.; Feng, W.; Zhang, H.-P.; Liu, H.-C.; Yan, C.-H. Shape-Selective Synthesis and Oxygen Storage Behavior of Ceria Nanopolyhedra, Nanorods, and Nanocubes. *J. Phys. Chem. B* **2005**, *109* (51), 24380–24385.

(24) Wu, Q.; Zhang, F.; Xiao, P.; Tao, H.; Wang, X.; Hu, Z.; Lü, Y. Great Influence of

Anions for Controllable Synthesis of CeO_2 Nanostructures: From Nanorods to Nanocubes. *J. Phys. Chem. C* **2008**, *112* (44), 17076–17080.

(25) Esch, F.; Fabris, S.; Zhou, L.; Montini, T.; Africh, C.; Fornasiero, P.; Comelli, G.; Rosei, R. Electron Localization Determines Defect Formation on Ceria Substrates. *Science (80-.).* **2005**, *309* (5735), 752–755.

(26) Nolan, M. Healing of Oxygen Vacancies on Reduced Surfaces of Gold-Doped Ceria. *J. Chem. Phys.* **2009**, *130* (14), 144702.

(27) Kullgren, J.; Hermansson, K.; Broqvist, P. Reactive Oxygen Species in Stoichiometric Ceria: Bulk and Low-Index Surfaces. *Phys. Status Solidi RRL* **2014**, *8* (6), 600–604.

(28) Nolan, M.; Fearon, J.; Watson, G. Oxygen Vacancy Formation and Migration in Ceria. *Solid State Ionics* **2006**, *177* (35–36), 3069–3074.

(29) Sun, L.; Huang, X.; Wang, L.; Janotti, A. Disentangling the Role of Small Polarons and Oxygen Vacancies in CeO_2. *Phys. Rev. B* **2017**, *95* (24), 245101.

(30) Chen, H.-T.; Chang, J.-G. Oxygen Vacancy Formation and Migration in $Ce_{1-x}Zr_xO_2$ Catalyst: A DFT+U Calculation. *J. Chem. Phys.* **2010**, *132* (21), 214702.

(31) Zhang, D.; Han, Z.-K.; Murgida, G. E.; Ganduglia-Pirovano, M. V.; Gao, Y. Oxygen-Vacancy Dynamics and Entanglement with Polaron Hopping at the Reduced CeO_2(111) Surface. *Phys. Rev. Lett.* **2019**, *122* (9), 096101.

(32) Lee, Y.; He, G.; Akey, A. J.; Si, R.; Flytzani-Stephanopoulos, M.; Herman, I. P. Raman Analysis of Mode Softening in Nanoparticle $CeO_{2-\delta}$ and Au-$CeO_{2-\delta}$ during CO Oxidation. *J. Am. Chem. Soc.* **2011**, *133* (33), 12952–12955.

(33) Guo, M.; Lu, J.; Wu, Y.; Wang, Y.; Luo, M. UV and Visible Raman Studies of Oxygen Vacancies in Rare-Earth-Doped Ceria. *Langmuir* **2011**, *27* (7), 3872–3877.

(34) Popović, Z. V.; Dohčević-Mitrović, Z.; Konstantinović, M. J.; Šćepanović, M. Raman Scattering Characterization of Nanopowders and Nanowires (Rods). *J. Raman Spectrosc.* **2007**, *38* (6), 750–755.